nature materials

LETTERS

PUBLISHED ONLINE: 7 MARCH 2016 | DOI: 10.1038/NMAT4589

Scalable water splitting on particulate photocatalyst sheets with a solar-to-hydrogen energy conversion efficiency exceeding 1%

Qian Wang[1,2], Takashi Hisatomi[1,2], Qingxin Jia[1,2], Hiromasa Tokudome[2,3], Miao Zhong[1,2], Chizhong Wang[1], Zhenhua Pan[1], Tsuyoshi Takata[4], Mamiko Nakabayashi[5], Naoya Shibata[5], Yanbo Li[6], Ian D. Sharp[6], Akihiko Kudo[7], Taro Yamada[1,2] and Kazunari Domen[1,2]*

Photocatalytic water splitting using particulate semiconductors is a potentially scalable and economically feasible technology for converting solar energy into hydrogen[1–3]. *Z*-scheme systems based on two-step photoexcitation of a hydrogen evolution photocatalyst (HEP) and an oxygen evolution photocatalyst (OEP) are suited to harvesting of sunlight because semiconductors with either water reduction or oxidation activity can be applied to the water splitting reaction[4,5]. However, it is challenging to achieve efficient transfer of electrons between HEP and OEP particles[6,7]. Here, we present photocatalyst sheets based on La- and Rh-codoped $SrTiO_3$ ($SrTiO_3$:La,Rh; ref. 8) and Mo-doped $BiVO_4$ ($BiVO_4$:Mo) powders embedded into a gold (Au) layer. Enhancement of the electron relay by annealing and suppression of undesirable reactions through surface modification allow pure water (pH 6.8) splitting with a solar-to-hydrogen energy conversion efficiency of 1.1% and an apparent quantum yield of over 30% at 419 nm. The photocatalyst sheet design enables efficient and scalable water splitting using particulate semiconductors.

The photocatalyst sheet presented in this work, which consists of $SrTiO_3$:La,Rh (La/(La+Sr) = Rh/(Rh+Ti) = 4 mol%) as a HEP and $BiVO_4$:Mo (Mo/V = 0.05 mol%) as an OEP embedded into a Au layer, is hereafter abbreviated as $SrTiO_3$:La,Rh/Au/$BiVO_4$:Mo. This sheet was fabricated by the particle transfer method (Fig. 1a and Methods; refs 9,10). In this process, both $SrTiO_3$:La,Rh and $BiVO_4$:Mo particles were embedded into a gold layer, as seen in the top-view scanning electron microscopy and energy dispersive X-ray fluorescence spectroscopy (SEM–EDX) mapping images of the $SrTiO_3$:La,Rh/Au/$BiVO_4$:Mo photocatalyst sheet (Fig. 1b–f). Photodeposition was then used to modify the photocatalyst sheet with Ru species as a co-catalyst[11]. Nanoparticulate Ru species were deposited on the surfaces of $SrTiO_3$:La,Rh and $BiVO_4$:Mo particles, as shown in Supplementary Fig. 1, and were probably attributable to Ru and RuO_x, respectively, by X-ray photoelectron spectroscopy (XPS) analysis (see Supplementary Fig. 2 and the accompanying discussion) and the Pourbaix diagram of Ru in water system[12].

The mechanism involved in the water splitting reaction on the $SrTiO_3$:La,Rh/Au/$BiVO_4$:Mo sheet is illustrated in Fig. 1g (ref. 9). When $SrTiO_3$:La,Rh/Au/$BiVO_4$:Mo is irradiated with visible light, photoexcited electrons are generated in the conduction bands of $SrTiO_3$:La,Rh and $BiVO_4$:Mo, whereas positive holes are generated in the donor levels formed by Rh^{3+} ions of $SrTiO_3$:La,Rh and in the valence band of $BiVO_4$:Mo. Electron transfer occurs from the conduction band of $BiVO_4$:Mo to the donor levels of $SrTiO_3$:La,Rh via gold. Meanwhile, the excited electrons in $SrTiO_3$:La,Rh reduce water to hydrogen on Ru species serving as a hydrogen evolution co-catalyst, and holes in $BiVO_4$ oxidize water to oxygen with the aid of RuO_x species functioning as an oxygen evolution co-catalyst, achieving overall water splitting. Therefore, the ability of the photocatalyst sheet for overall water splitting should be promoted by facilitating charge transfer through the underlying Au layer. Note that the Au layer is too thick (approximately 350 nm) to induce the surface plasmon resonance below 520 nm, where the $SrTiO_3$:La,Rh/Au/$BiVO_4$:Mo system shows water splitting activity[9].

To reduce the contact resistance between the semiconductors and the metal layer, the photocatalyst sheet samples were annealed in air[13,14]. The activity in *Z*-scheme water splitting was indeed strongly dependent on the annealing temperature and duration, as shown in Fig. 1h and Supplementary Fig. 3; it was maximized (almost doubled) on annealing at 573 K for 20 min. The sample annealed before the deposition of Au (referred to as 'pre-annealed') exhibited similar gas evolution rates to the unannealed sample (Supplementary Fig. 4). This rules out the possibility that the heat treatment intensified the junction between the two kinds of semiconductor particles or altered the semiconducting properties of the photocatalysts favourably. The effect of annealing was further investigated through photoelectrochemical measurements of $SrTiO_3$:La,Rh/Au and $BiVO_4$:Mo/Au electrodes. The $SrTiO_3$:La,Rh/Au and $BiVO_4$:Mo/Au electrodes generated cathodic and anodic photocurrents, respectively (see Supplementary Fig. 5 and the accompanying discussion). Compared with the pristine electrodes, the electrodes annealed at 573 K for 20 min generated almost twice the photocurrent. These results indicate that the resistance between $SrTiO_3$:La,Rh and $BiVO_4$:Mo particles via the Au layer was reduced by annealing at 573 K for 20 min. However,

[1]Department of Chemical System Engineering, School of Engineering, The University of Tokyo, 7-3-1 Hongo, Bunkyo-ku, Tokyo 113-8656, Japan. [2]Japan Technological Research Association of Artificial Photosynthetic Chemical Process (ARPChem), 5-1-5 Kashiwanoha, Kashiwa-shi, Chiba 277-8589, Japan. [3]Research Institute, TOTO Ltd., 2-8-1 Honson, Chigasaki, Kanagawa 253-8577, Japan. [4]Global Research Center for Environment and Energy Based on Nanomaterials Science (GREEN), National Institute for Materials Science (NIMS), 1-1 Namiki, Tsukuba-shi, Ibaraki 305-0044, Japan. [5]Institute of Engineering Innovation, The University of Tokyo, 2-11-16 Yayoi, Bunkyo-ku, Tokyo 113-8656, Japan. [6]Joint Center for Artificial Photosynthesis, Lawrence Berkeley National Laboratory, 1 Cyclotron Road, Berkeley, California 94720, USA. [7]Department of Applied Chemistry, Tokyo University of Science, 1-3 Kagurazaka, Shinjuku-ku, Tokyo 162-8601, Japan. *e-mail: domen@chemsys.t.u-tokyo.ac.jp

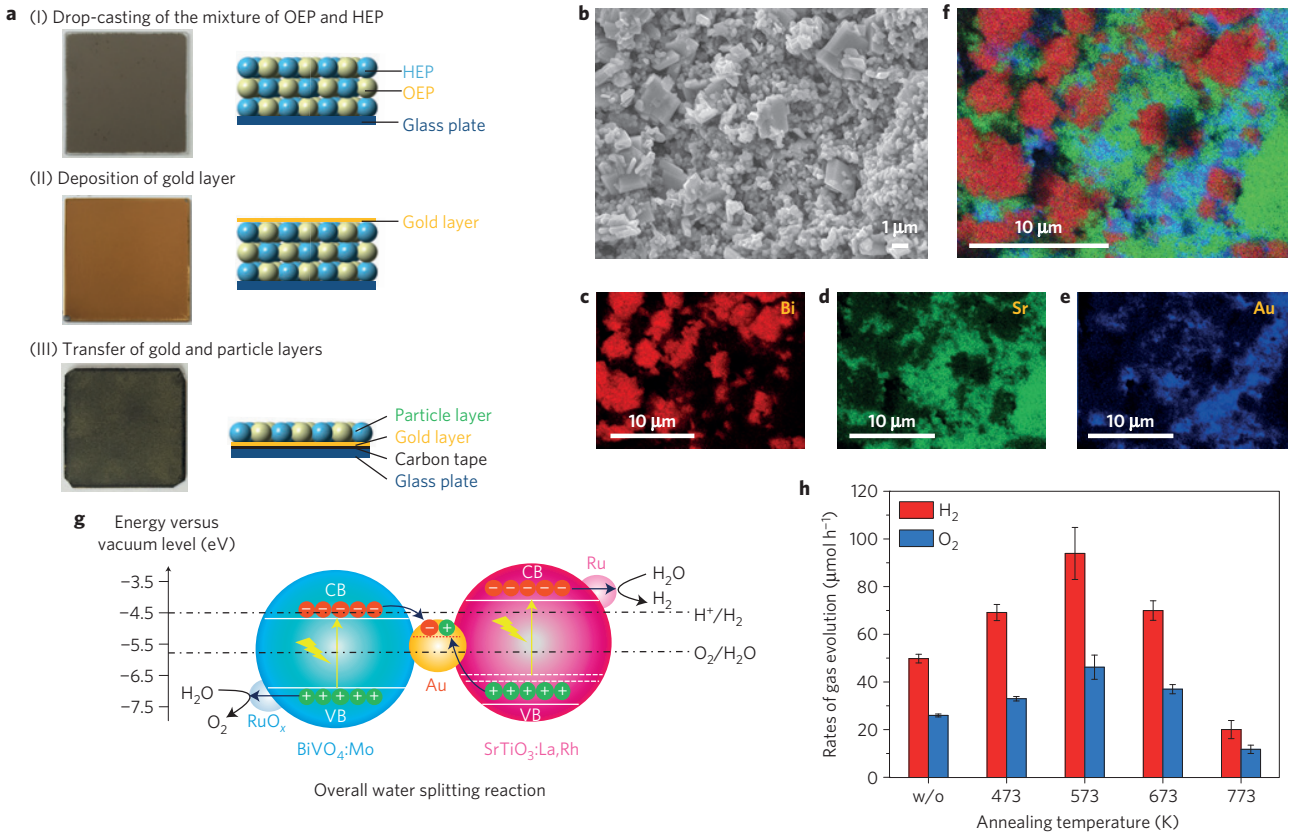

Figure 1 | $SrTiO_3$:La,Rh/Au/$BiVO_4$:Mo sheet prepared by particle transfer method. a, Illustration of the preparation of the $SrTiO_3$:La,Rh/Au/$BiVO_4$:Mo sheet by the particle transfer method. **b**–**f**, Top-view SEM–EDX elemental mapping images showing an SEM image (**b**), Bi distribution (**c**), Sr distribution (**d**), Au distribution (**e**), and a superimposition of the distributions (**f**). **g**, Schematic of overall water splitting on the Ru-modified $SrTiO_3$:La,Rh/Au/$BiVO_4$:Mo sheet. CB, conduction band; VB, valence band. **h**, Dependence of overall water splitting activity of Ru-modified $SrTiO_3$:La,Rh/Au/$BiVO_4$:Mo photocatalyst sheets on annealing temperature. All samples were annealed for 20 min. 'w/o' stands for the pristine sample. The error bars show the standard deviations. Reactions were carried out under Xe lamp (300 W) illumination ($\lambda > 420$ nm) at 288 K and 5 kPa.

the water splitting activity decreased sharply when the sample was heated at higher temperatures (673–773 K) and/or for longer durations (30 min), probably because of the volatilization of V_2O_5 (refs 15,16). EDX analysis (Supplementary Table 1) revealed that the Bi/V molar ratio of excessively heated samples exceeded that for stoichiometric $BiVO_4$ (Bi/V = 1). These samples exhibited a lighter yellow colour than the other samples, as illustrated in Supplementary Fig. 6. Notably, the Au layer deposited by electron beam evaporation under heating *in vacuo* tended to produce approximately 20% higher water splitting activity than that deposited by vacuum evaporation without substrate heating. This is probably due to the *in situ* desorption of adsorbents on the photocatalyst particles before Au deposition.

The overall water splitting rate on the Ru-modified $SrTiO_3$:La,Rh/Au/$BiVO_4$:Mo sheet (7.5 cm^2) annealed at 573 K for 20 min was maximized when the amount of $RuCl_3$ added was 0.2 μmol (Supplementary Fig. 7), because the Ru species loaded on the photocatalysts not only served as co-catalysts but also blocked incident photons[11]. The solar-to-hydrogen energy conversion efficiency (STH) of the optimally modified sample was 0.29% at 288 K in the initial three hours of the reaction (Supplementary Fig. 8). However, it was noted that the water splitting reaction competed with the formation of water from hydrogen and oxygen and the photoreduction of oxygen molecules, typical backward reactions, on the Ru-modified $SrTiO_3$:La,Rh/Au/$BiVO_4$:Mo sheet. The water splitting rate decreased with irradiation time, although it recovered on degassing the reaction system (Supplementary Fig. 8). In addition, the photocatalytic water splitting activity dropped to 23% and 10% when the background reaction pressure was increased from 5 to 10 and 20 kPa, respectively (Supplementary Fig. 9), because the hydrogen and oxygen bubbles needed larger numbers of gas molecules to desorb from the photocatalyst sheet at a higher background pressure.

We previously found that Cr_2O_3 shell capping noble metal nanoparticles suppressed the backward reactions whilst maintaining the function of the noble metal as a hydrogen evolution catalyst[17,18]. Hence, Cr_2O_3 was deposited on the Ru-modified $SrTiO_3$:La,Rh/Au/$BiVO_4$:Mo sheet sample by photodeposition. The activity improved with increasing amount of K_2CrO_4 up to 0.1 μmol for 7.5 cm^2-sized samples (Supplementary Fig. 10). More importantly, after the photodeposition of Cr_2O_3, the photocatalyst sheet sample maintained a water splitting activity of 78% and 60% at 10 and 20 kPa, respectively (Supplementary Fig. 9). No noticeable decrease in photocatalytic activity was observed for at least 10 h (Fig. 2a). Moreover, an additional surface modification by recently developed amorphous titanium oxide (a-TiO_2) layers[19,20] suppressed the background pressure effect further. The photocatalyst sheet samples modified with the Cr_2O_3 and a-TiO_2 layers maintained a water splitting activity of 89% and 86% at 10 and 20 kPa, respectively (Supplementary Fig. 9). Suppression of the backward reactions is a critical factor for the activity of photocatalyst sheets because hydrogen and oxygen are generated in close proximity. Hence, the water splitting reaction was carried out at low background pressures at present. However, this problem can be overcome through the development of surface modifications suppressing the backward reactions effectively.

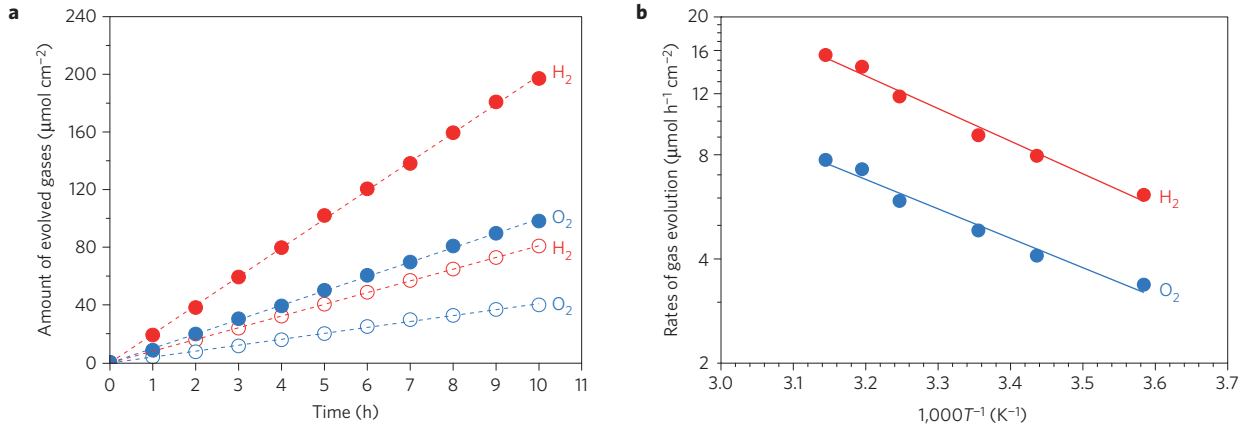

Figure 2 | Effect of reaction temperature on photocatalytic water splitting rate of the $SrTiO_3$:La,Rh/Au/$BiVO_4$:Mo sheet. a, Time courses of the water splitting reaction on a Cr_2O_3/Ru-modified $SrTiO_3$:La,Rh/Au/$BiVO_4$:Mo sheet under simulated sunlight (AM 1.5G) at 288 K and 5 kPa (open symbols) and 331 K and 10 kPa (closed symbols). **b**, Temperature (T) dependence of the water splitting activity of the Cr_2O_3/Ru-loaded $SrTiO_3$:La,Rh/Au/$BiVO_4$:Mo photocatalyst sheet at a background pressure of 5 kPa under AM 1.5G simulated sunlight. The Au layer was deposited by electron beam evaporation.

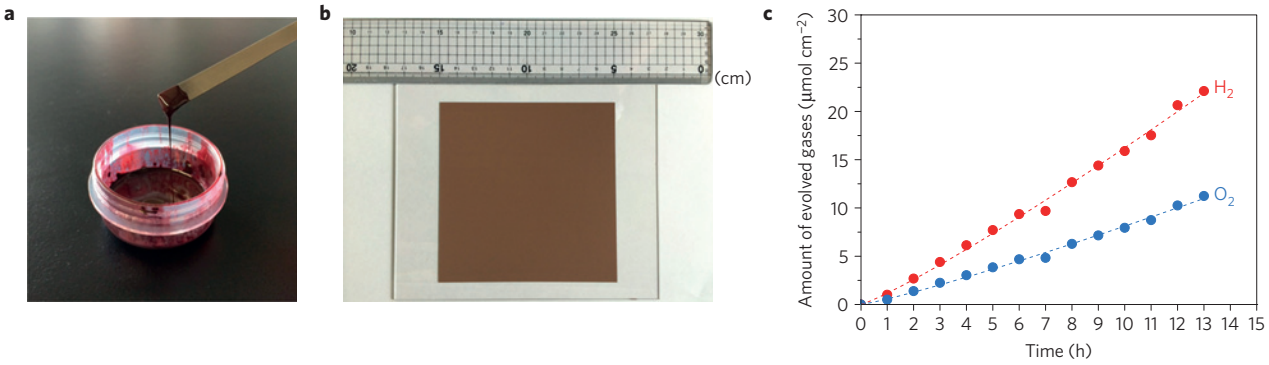

Figure 3 | Printed photocatalyst sheet. a, Photograph of the ink used for screen printing the photocatalyst sheet. **b**, Photograph of a 10 × 10 cm $SrTiO_3$:La,Rh/Au nanoparticle/$BiVO_4$:Mo printed sheet. **c**, Time course of the water splitting reaction using a Ru-modified $SrTiO_3$:La,Rh/Au colloid (40 wt%)/$BiVO_4$:Mo printed sheet under simulated sunlight at 288 K and 5 kPa. The sample (6.25 cm^2) was photodeposited with $RuCl_3 \cdot 3H_2O$ (0.17 μmol).

Figure 2b shows the reaction temperature dependence of the photocatalytic water splitting rate on $SrTiO_3$:La,Rh/Au/$BiVO_4$:Mo modified with the co-catalyst Cr_2O_3/Ru. The water splitting reaction was enhanced monotonically with increasing reaction temperature in the range from 279 to 318 K at a background pressure of 5 kPa. The apparent activation energy of the overall water splitting reaction was 18 kJ mol^{-1}, which was higher than that observed for $Rh_{2-y}Cr_yO_3$-loaded $(Ga_{1-x}Zn_x)(N_{1-x}O_x)$ (8 kJ mol^{-1}; refs 21,22). It is plausible that electron transfer across the Schottky barrier at the $BiVO_4$:Mo/Au interface and hole transfer through the donor levels formed by Rh^{3+} ions in $SrTiO_3$:La,Rh necessitate thermal excitation for effective conduction. Note that the reaction temperature can reach about 333 K under solar illumination in practical operating conditions[23–25]. The STH of the pure water (pH 6.8) splitting reaction using a Cr_2O_3/Ru-loaded $SrTiO_3$:La,Rh/Au/$BiVO_4$:Mo sheet was 1.0% at 318 K at a background pressure of 5 kPa. Under simulated sunlight (AM 1.5 G) irradiation through Pyrex glass, hydrogen and oxygen bubbles evolved vigorously on the photocatalyst sheet immersed in pure water (pH 6.8) and the gas evolution ceased immediately when the illumination was interrupted, as presented in Supplementary Movie 1 with the original playing speed. The apparent quantum yield (AQY) and STH reached 33% at 419 nm and 1.1%, respectively, at 331 K and 10 kPa (Fig. 2a). By comparison, the photocatalyst suspension Z-scheme system consisting of $SrTiO_3$:Rh and $BiVO_4$ powders and $Fe^{3+/2+}$ redox couples exhibited an AQY of 4.2% at 420 nm and an STH of 0.1% under the best reaction conditions[26]. Clearly, the photocatalyst sheet recorded by far the highest AQY and STH amongst Z-scheme water splitting systems based on particulate semiconductors, in the absence of any external bias. Higher STHs were reported for photocatalytic water splitting on single materials such as CoO (ref. 27) and CDots/C_3N_4 (ref. 28), although further studies seem to be necessary to confirm the reproducibility.

The present photocatalyst sheet design can be extended to scalable solution processes—for example, screen printing of ink containing an HEP, OEP, and colloidal conductor such as Au and indium tin oxide (Fig. 3a and Methods)—as long as the HEP and OEP particles are bridged in proximity. This is because, unlike in (photo)electrochemical systems, a continuous conductive layer is not needed, owing to the absence of an external electric circuit. Indeed, a 10 × 10 cm printed photocatalyst sheet was readily prepared by the screen-printing method, as shown in Fig. 3b. In a printed $SrTiO_3$:La,Rh/Au colloid (10 wt%)/$BiVO_4$:Mo photocatalyst sheet, Au nanoparticles with sizes ranging from several nanometres to 50 nm were dispersed on the surfaces of the $SrTiO_3$:La,Rh and $BiVO_4$:Mo particles, as shown in Supplementary Fig. 11. Au nanoparticles aggregated in significant numbers and bridged the HEP and OEP particles effectively (Supplementary Fig. 12). The printed $SrTiO_3$:La,Rh/Au colloid/$BiVO_4$:Mo sheet produced hydrogen and oxygen from pure water (pH 6.8) in the stoichiometric ratio. The water splitting activity of the printed sheet (Supplementary Fig. 13) was enhanced with increasing amounts

of Au colloid up to 40 wt%, indicating that Au nanoparticle agglomerates effectively served as an electron conductor between $BiVO_4$:Mo and $SrTiO_3$:La,Rh. The STH of the Ru-loaded printed $SrTiO_3$:La,Rh/Au colloid (40 wt%)/$BiVO_4$:Mo sheet was 0.1% on the basis of the average gas evolution rate during the 13-h reaction (Fig. 3c). This value was rather low because of the difficulty in photodepositing co-catalysts on a thick particle layer (approximately 10 μm) and the presence of a large amount of Au. Nevertheless, the STH obtained here is still very high compared to those of previously reported particulate photocatalytic systems[6–8] operating in pure water.

It is notable that the photocatalyst sheet exhibited a high water splitting activity in pure water without any supporting electrolytes, buffering reagents, pH adjustment, or applied voltage. On the photocatalyst sheet sample, HEP and OEP particles are physically embedded into a conductor in the immediate vicinity. This configuration is effective in suppressing the generation of concentration overpotentials of H^+/OH^- and *IR* drops between the hydrogen and oxygen evolution sites commonly observed in (photo)electrochemical water splitting. Therefore, the photocatalyst sheet with high activity is scalable as is. Another key advance in photocatalyst sheet systems demonstrated by the present study is the facilitation of electron transfer between HEP and OEP by conductor layers or particles. In the $SrTiO_3$:La,Rh/Au/$BiVO_4$:Mo photocatalyst sheet system, the annealing-induced enhancement in the electric contact between Au and the semiconductor photocatalysts boosted the gas evolution rates, confirming the importance of electron transfer through the Au layer. In addition, modification of the Ru catalyst with Cr_2O_3 and a-TiO_2 layers effectively suppressed the backward reactions, allowing the photocatalyst sheet systems to maintain a high activity at elevated pressures. The photocatalyst sheet system based on simple and versatile technologies greatly extends the potential of particulate photocatalysts in efficient solar hydrogen production from pure water on a large scale. A gaseous mixture of hydrogen and oxygen is produced on the photocatalyst sheet, but this can be separated safely by introducing the molecular sieving effect of microporous membranes into the system, with a minimum energy loss of 1.1% (refs 29,30). Photocatalyst sheet designs with a relatively low cost could thus lead to advances that would enable industrial solar hydrogen production. The STH of the present $SrTiO_3$:La,Rh/Au/$BiVO_4$:Mo system is limited by the short absorption edge wavelengths of $SrTiO_3$:La,Rh and $BiVO_4$:Mo (520 and 540 nm, respectively). Also, the use of Au as a conductor is an economic obstacle to scaling up. The potential of photocatalyst sheet systems can be further extended by employing particulate photocatalysts with narrower bandgap energies and inexpensive conducting materials.

In conclusion, we demonstrated efficient and scalable systems for *Z*-scheme pure water splitting based on particulate photocatalyst sheets. The $SrTiO_3$:La,Rh/Au/$BiVO_4$:Mo photocatalyst sheet exhibited an AQY of 33% at 419 nm and an STH of 1.1% in overall pure water (pH 6.8) splitting. Moreover, a photocatalyst sheet prepared by screen printing an ink containing $SrTiO_3$:La,Rh, $BiVO_4$:Mo, and a Au colloid exhibited an STH of 0.1%.

Methods

Methods and any associated references are available in the online version of the paper.

Received 20 August 2015; accepted 26 January 2016; published online 7 March 2016

References

1. Chen, X., Shen, S., Guo, L. & Mao, S. Semiconductor-based photocatalytic hydrogen generation. *Chem. Rev.* **110,** 6503–6570 (2010).
2. Walter, M. G. *et al*. Solar water splitting cells. *Chem. Rev.* **110,** 6446–6473 (2010).
3. Pinaud, B. A. *et al*. Technical and economic feasibility of centralized facilities for solar hydrogen production via photocatalysis and photoelectrochemistry. *Energy Environ. Sci.* **6,** 1983–2002 (2013).
4. Hisatomi, T., Kubota, J. & Domen, K. Recent advances in semiconductors for photocatalytic and photoelectrochemical water splitting. *Chem. Soc. Rev.* **43,** 7520–7535 (2014).
5. Yuan, Y.-P., Ruan, L.-W., Barber, J., Joachim Loo, S. C. & Xue, C. Hetero-nanostructured suspended photocatalysts for solar-to-fuel conversion. *Energy Environ. Sci.* **7,** 3934–3951 (2014).
6. Maeda, K. *Z*-scheme water splitting using two different semiconductor photocatalysts. *ACS Catal.* **3,** 1486–1503 (2013).
7. Sasaki, Y., Nemoto, H., Saito, K. & Kudo, A. Solar water splitting using powdered photocatalysts driven by *Z*-schematic interparticle electron transfer without an electron mediator. *J. Phys. Chem. C* **113,** 17536–17542 (2009).
8. Wang, Q., Hisatomi, T., Ma, S. S. K., Li, Y. & Domen, K. Core/shell structured La- and Rh-codoped $SrTiO_3$ as a hydrogen evolution photocatalyst in *Z*-scheme overall water splitting under visible light irradiation. *Chem. Mater.* **26,** 4144–4150 (2014).
9. Wang, Q. *et al*. *Z*-scheme water splitting using particulate semiconductors immobilized onto metal layers for efficient electron relay. *J. Catalys.* **328,** 308–315 (2015).
10. Minegishi, T., Nishimura, N., Kubota, J. & Domen, K. Photoelectrochemical properties of $LaTiO_2N$ electrodes prepared by particle transfer for sunlight-driven water splitting. *Chem. Sci.* **4,** 1120–1124 (2013).
11. Sasaki, Y., Iwase, A., Kato, H. & Kudo, A. The effect of co-catalyst for *Z*-scheme photocatalysis systems with an Fe^{3+}/Fe^{2+} electron mediator on overall water splitting under visible light irradiation. *J. Catalys.* **259,** 133–137 (2008).
12. Piela, P., Eickes, C., Brosha, E., Garzon, F. & Zelenay, P. Ruthenium crossover in direct methanol fuel cell with Pt-Ru black anode. *J. Electrochem. Soc.* **151,** A2053–A2059 (2004).
13. Luther, B. *et al*. Investigation of the mechanism for ohmic contact formation in Al and Ti/Al contacts to n-type GaN. *Appl. Phys. Lett.* **70,** 57–59 (1997).
14. Hsu, C.-Y., Lan, W.-H. & Wu, Y. S. Effect of thermal annealing of Ni/Au ohmic contact on the leakage current of GaN based light emitting diodes. *Appl. Phys. Lett.* **83,** 2447–2449 (2003).
15. Kudo, A., Omori, K. & Kato, H. A novel aqueous process for preparation of crystal form-controlled and highly crystalline $BiVO_4$ powder from layered vanadates at room temperature and its photocatalytic and photophysical properties. *J. Am. Chem. Soc.* **121,** 11459–11467 (1999).
16. Berglund, S. P., Flaherty, D. W., Hahn, N. T., Bard, A. J. & Mullins, C. B. Photoelectrochemical oxidation of water using nanostructured $BiVO_4$ films. *J. Phys. Chem. C* **115,** 3794–3802 (2011).
17. Maeda, K. *et al*. Noble-metal/Cr_2O_3 core/shell nanoparticles as a cocatalyst for photocatalytic overall water splitting. *Angew. Chem. Int. Ed.* **45,** 7806–7809 (2006).
18. Yoshida, M. *et al*. Role and function of noble-metal/Cr-layer core/shell structure cocatalysts for photocatalytic overall water splitting studied by model electrodes. *J. Phys. Chem. C* **113,** 10151–10157 (2009).
19. Takata, T., Pan, C., Nakabayashi, M., Shibata, N. & Domen, K. Fabrication of a core-shell-type photocatalyst via photodeposition of group IV and V transition metal oxyhydroxides: an effective surface modification method for overall water splitting. *J. Am. Chem. Soc.* **137,** 9627–9634 (2015).
20. Xu, J., Pan, C., Takata, T. & Domen, K. Photocatalytic overall water splitting on the perovskite-type transition metal oxynitride $CaTaO_2N$ under visible light irradiation. *Chem. Commun.* **51,** 7191–7194 (2015).
21. Dionigi, F. *et al*. Gas phase photocatalytic water splitting with $Rh_{2-y}Cr_yO_3$/GaN:ZnO in μ-reactors. *Energy Environ. Sci.* **4,** 2937–2942 (2011).
22. Hisatomi, T., Minegishi, T. & Domen, K. Kinetic assessment and numerical modeling of photocatalytic water splitting toward efficient solar hydrogen production. *Bull. Chem. Soc. Jpn* **85,** 647–655 (2012).
23. Wohlgemuth, J. H., Cunningham, D. W., Monus, P., Miller, J. & Nguyen, A. Long term reliability of photovoltaic modules. In *Conference Record of the 2006 IEEE 4th World Conference on Photovoltaic Energy Conversion* Vol. 2, 2050–2053 (IEEE, 2006).
24. Kurtz, S. *et al*. Evaluation of high-temperature exposure of photovoltaic modules. *Prog. Photovolt. Res. Appl.* **19,** 954–965 (2011).
25. Pihosh, Y. *et al*. Photocatalytic generation of hydrogen by core-shell $WO_3/BiVO_4$ nanorods with ultimate water splitting efficiency. *Sci. Rep.* **5,** 11141 (2015).
26. Kato, H., Sasaki, Y., Shirakura, N. & Kudo, A. Synthesis of highly active rhodium-doped $SrTiO_3$ powders in *Z*-scheme systems for visible-light-driven photocatalytic overall water splitting. *J. Mater. Chem. A* **1,** 12327–12333 (2013).
27. Liao, L. *et al*. Efficient solar water-splitting using a nanocrystalline CoO photocatalyst. *Nature Nanotech.* **9,** 69–73 (2014).

28. Liu, J. *et al*. Metal-free efficient photocatalyst for stable visible water splitting via a two-electron pathway. *Science* **347,** 970–974 (2015).
29. Caro, J. & Noack, M. Zeolite membranes—Recent deveopments and progress. *Micropor. Mesopor. Mater.* **115,** 215–233 (2008).
30. Li, H., Haas-Santo, K., Schygulla, U. & Dittmeyer, R. Inorganic microporous membranes for H_2 and CO_2 separation—Review of experimental and modeling progress. *Chem. Eng. Sci.* **127,** 401–417 (2015).

Acknowledgements

This work was financially supported by the Artificial Photosynthesis Project of the New Energy and Industrial Technology Development Organization (NEDO), by Grants-in-Aids for Specially Promoted Research (No. 23000009) and for Young Scientists (A) (No. 15H05494), and the A3 Foresight Program of Japan Society for the Promotion of Science (JSPS). A part of this work was conducted at Research Hub for Advanced Nano Characterization, The University of Tokyo, with the support of the Ministry of Education, Culture, Sports, Science and Technology (MEXT), Japan. T.T. performed work at GREEN, NIMS supported through the Development of Environmental Technology using Nanotechnology from the Ministry of Education, Culture, Sports, Science and Technology (MEXT). I.D.S. and Y.L. performed work at the Joint Center for Artificial Photosynthesis, a DOE Energy Innovation Hub, supported through the Office of Science of the US Department of Energy under Award Number DE-SC0004993.

Author contributions

Q.W., T.H., Y.L. and K.D. conceived the photocatalyst sheet design. Q.W. prepared $SrTiO_3$:La,Rh and the photocatalyst sheet, conducted XRD, DRS, XPS and SEM characterizations and the water splitting reactions. T.H. and K.D. supervised the experimental work. Q.J. prepared the $BiVO_4$:Mo particles. H.T. prepared the printed photocatalyst sheets. M.Z. and C.W. performed the photoelectrochemical measurements. Q.W., Z.P. and T.T. conducted the surface modification with a-TiO_2. M.N. and N.S. conducted the SEM–EDX elemental mapping measurements. Q.W., Y.L. and I.D.S. carried out the electron beam evaporation. Q.W., T.H., Q.J., H.T., Y.L., A.K., T.Y. and K.D. discussed the results. Q.W. and T.H. wrote the manuscript with contributions from the other co-authors.

Additional information

Supplementary information is available in the online version of the paper. Reprints and permissions information is available online at www.nature.com/reprints. Correspondence and requests for materials should be addressed to K.D.

Competing financial interests

The authors declare no competing financial interests.

Methods

Synthesis of $SrTiO_3$:La,Rh and $BiVO_4$:Mo particles. $SrTiO_3$:La,Rh (La/(La+Sr) = Rh/(Rh+Ti) = 4 mol%) was synthesized by a two-step solid state reaction (SSR; ref. 8). In the initial step, $SrTiO_3$ was prepared by a conventional SSR. $SrCO_3$ (Kanto Chemicals, 99.9%, heated in air at 573 K for 1 h before use) and rutile-type TiO_2 (Kanto Chemicals, 99.0%) powders were mixed in a mortar at a Sr/Ti ratio of 1.05 and calcined at 1,423 K for 10 h. Subsequently, the resulting $SrTiO_3$ was mixed in ethanol with La_2O_3 (Kanto Chemicals, 99.99%, freshly calcined in air at 1,273 K for 12 h before use) and Rh_2O_3 (Kanto Chemicals, 99.9%) and heated at 1,373 K for 6 h.

$BiVO_4$:Mo (Mo/V = 0.05 mol%) was synthesized through aqueous processes[15]. Layered Mo-doped $K_3V_5O_{14}$ was prepared as a precursor by calcining a mixture of K_2CO_3 (Kanto Chemical, 99.5%), MoO_3 (Kanto Chemical, 99.5%) and V_2O_5 (Wako Pure Chemical, 99.0%) in air at 723 K for 5 h. A suspension of $BiONO_3$ was prepared by adding $Bi(NO_3)_3 \cdot 5H_2O$ (Kanto Chemical, 99.9%) in distilled water. Mo-doped $K_3V_5O_{14}$ was added to the suspension of $BiONO_3$, and the suspension was stirred mildly at 343 K for 10 h. The resulting $BiVO_4$:Mo (Mo/V = 0.05 mol%) was collected by filtration and washed with distilled water.

The morphologies of the produced samples were characterized by the scanning electron microscope (SEM) images (Supplementary Fig. 1). The phases of the samples were confirmed from the X-ray diffraction (XRD) patterns (Supplementary Fig. 14). The diffuse reflectance spectra (DRS) of the prepared samples are shown in Supplementary Fig. 15.

Preparation of $SrTiO_3$:La,Rh/Au/$BiVO_4$:Mo photocatalyst sheets. $SrTiO_3$:La,Rh/Au layer/$BiVO_4$:Mo photocatalyst sheets were fabricated by the particle transfer method[9,10] by the following procedure: first, a mixture of $SrTiO_3$:La,Rh and $BiVO_4$:Mo powders (10 mg each) at the optimized mass ratio of 1:1 (Supplementary Fig. 16) was suspended in isopropanol (99.9%, 0.5 ml) and drop-cast on a glass substrate (3 × 3 cm); then, after drying at room temperature, a thin gold layer (~350 nm) was deposited by thermal vacuum evaporation (VFR-200M/ERH, ULVAC KIKO) at an evaporation rate of approximately 20 nm s^{-1} under a base pressure of 2.6×10^{-3} Pa or electron beam evaporation (Nexdep, Angstrom Engineering) at an evaporation rate of 2 Å s^{-1} after the chamber was evacuated to a pressure of 2.9×10^{-4} Pa and the substrate was heated to 673 K; next, the sample was placed on an alumina plate, heated to 473–773 K at 10 K min^{-1} and kept at the target temperature for 10–30 min; then, the Au film holding the particulate photocatalysts was bonded to a second glass plate (about 3 × 3 cm) with an adhesive carbon tape and then lifted off the primary glass plate; and finally the photocatalyst sheet obtained was ultrasonicated twice, for 2 min each time, in distilled water to remove excess particles piling up on the particle layer, because outer layer photocatalyst particles which did not contact with the Au layer could have little contribution to the photocatalytic activity[9].

$SrTiO_3$:La,Rh/Au colloid/$BiVO_4$:Mo composite prints were fabricated by screen printing. The printing ink was prepared by mixing 60 mg of $SrTiO_3$:La,Rh powder, 60 mg of $BiVO_4$:Mo powder, 133–1,200 mg of Au colloid solution (average particle diameter ≈20 nm, 10 wt% in ethanol, AUSK-2000E, Shinko Kagaku) and 600 mg of an organic vehicle consisting of α-terpineol, 2-(2-butoxyethoxy)ethanol and acrylic resin ('SPB-TE1', Soken Chemicals and Engineering) at a weight ratio of 62.5:12.5:25.0. After evaporation of ethanol, the paste was screen printed on a glass substrate (about 3 × 3 cm). The printed area was controlled to be 2.5 × 2.5 cm for the measurement of photocatalytic activity. The obtained print was dried at 353 K for 30 min and calcined at 573 K for 30 min.

Preparation of photoelectrodes. Photoelectrodes of $SrTiO_3$:La,Rh/Au and $BiVO_4$:Mo/Au were fabricated by a particle transfer method similar to the fabrication of the photocatalyst sheet. $SrTiO_3$:La,Rh or $BiVO_4$:Mo powder (20 mg) was dispersed in isopropanol (0.5 ml) by ultrasonication for 30 min. The suspension was deposited on a glass substrate. Au layers 600–800 nm in thickness were deposited on the semiconductor particles by vacuum evaporation repeatedly to maintain the evaporation rate and operation pressure similar to the preparation process of the photocatalyst sheet. The deposited Au film was approximately 3 μm in thickness to ensure the continuity and conductivity. The resulting Au film holding the photocatalyst powder was annealed at 573 K for 20 min, peeled off, and processed into electrodes.

Characterization. The XRD patterns of the samples were measured with a Rigaku RINT-UltimaIII diffractometer using Cu Kα source operated at 40 kV and 40 mA. The DRS were obtained using an ultraviolet–visible–near-infrared spectrometer (V-670, JASCO) and were converted from reflection to absorbance by the Kubelka–Munk method. The SEM images were recorded on the Hitachi SU8020 system at an acceleration voltage of 3 kV. The XPS measurements were carried out using a monochromatic Mg Kα source ($h\nu$ = 1,253.6 eV) excited at 8 kV and 10 mA. The analysis chamber pressure was ~10^{-6} Pa. The binding energies were corrected using the C 1s peak (285.0 eV) as a reference. A JEOL JSM-7001FA system was used for the SEM–EDX elemental mapping.

Photoelectrochemical measurements. Photoelectrochemical water splitting properties of the $SrTiO_3$:La,Rh/Au and $BiVO_4$:Mo/Au photoelectrodes were investigated in the three-electrode configuration using a Ag/AgCl reference electrode (in saturated KCl aqueous solution) and a Pt wire counter electrode. The potential of the working electrode was controlled by a potentiostat (Hokuto Denko, HSV-100). The potential measured to the Ag/AgCl electrode was also expressed in the reversible hydrogen electrode (RHE) scale through calibration. An aqueous solution of 0.1 M Na_2SO_4 was used as an electrolyte solution under stirring and purging with Ar gas. The pH of the electrolyte solution was adjusted to 6.8 by adding H_2SO_4 (aq.) or NaOH (aq.) when necessary. The photoelectrodes were irradiated with a 300 W Xe lamp (Lamp house, R300-3J) equipped with a cutoff filter ($\lambda > 420$ nm). Current–potential curves were measured at a scan rate of 10 mV s^{-1} from negative to positive potential for the $BiVO_4$:Mo/Au photoanodes and in the reverse direction for $SrTiO_3$:La/Rh/Au photocathodes.

Photodeposition of co-catalysts and surface modifiers. The photocatalyst sheets were modified with nanoparticulate Ru species by photodeposition because Ru species was known to work more efficiently as a hydrogen evolution co-catalyst than other metal species in *Z*-scheme water splitting using $SrTiO_3$:Rh/$BiVO_4$ powder suspension[11]. Subsequently, the photocatalyst sheets were modified with Cr_2O_3 and a-TiO_2 layers successively by photodeposition to suppress the backward reactions. The Cr_2O_3 and a-TiO_2 layers can suppress the backward reactions because oxygen molecules in the reaction solution cannot penetrate the hydrated oxide layers to reach the nanoparticulate noble metal whereas protons and hydrogen molecules can[17–20].

In the first step, Ru species were photodeposited on the photocatalyst sheets from $RuCl_3 \cdot 3H_2O$ dissolved in distilled water (40 ml). In the second step, the reactant was changed to an aqueous K_2CrO_4 solution. The amounts of $RuCl_3 \cdot 3H_2O$ and K_2CrO_4 were 0.2 and 0.1 μmol for a photocatalyst sheet sample 7.5 cm^2 in size unless otherwise noted. In the third step, an a-TiO_2 layer was deposited from a Ti peroxide solution[20]. The Ti peroxide solution was prepared by the following procedures: titanium tetraisopropoxide (10 μl, Kanto Chemical, 97%) and H_2O_2 (25 μl, Wako Pure Chemical Industries, 30%) were added to distilled water (1 ml). The suspension was subjected to ultrasonication for a few minutes until it turned into a transparent yellow. The photodeposition reactions were conducted in a Pyrex top-irradiation reaction vessel connected to a glass closed gas circulation system. Argon gas was introduced into the circulation system as a carrier gas after removing the air. The total background pressure of argon and water vapour was approximately 5 kPa. The temperature of the reactant solution was maintained at 288 K by cooling water. Photodeposition was performed under a 300 W Xe lamp (Lamp House, R300-3J; irradiation spectra in Supplementary Fig. 17) equipped with a cutoff filter ($\lambda > 420$ nm) until steady gas evolution rates were obtained (typically for 5 h). The number of photons (420 nm < λ < 540 nm) incident on the photocatalyst sheet (7.5 cm^2) was measured using a grating spectroradiometer (EKO Instruments Co., Ltd., LS-100) to be 3.9×10^{21} photon h^{-1}. The amounts of gases produced were measured by gas chromatography (Shimadzu GC-8A with a TCD detector and MS-5A columns and argon carrier gas).

Overall water splitting reaction. *Z*-scheme water splitting reactions were carried out in the same closed gas circulation system with top illumination from a 300 W Xe lamp equipped with a cutoff filter ($\lambda > 420$ nm) or a solar simulator (Asahi Spectra, HAL-320; irradiation spectra in Supplementary Fig. 18). The photocatalyst sheet samples (about 7.5 cm^2) were placed at the bottom of the reaction cell containing pure water (40 ml). The reaction temperature was kept at 288 K and the background pressure was 5 kPa unless otherwise noted. The temperature of the reactant solution was raised (lowered) by a water (ice) bath.

Quantum yield measurement. The apparent quantum yield (AQY) of the *Z*-scheme water splitting based on a two-step photoexcitation process is given by equation (1):

$$\mathrm{AQY}(\%) = [4 \times n(\mathrm{H_2})]/n(\mathrm{photons}) \times 100 \quad (1)$$

where $n(H_2)$ and n(photons) denote the number of produced H_2 molecules and the number of incident photons, respectively. The water splitting reaction was carried out using the same experimental set-up, except for the use of a bandpass filter with central wavelength of 418.6 nm and full-width at half-maximum of 9.5 nm. The spatial distributions of the power spectra are presented in Supplementary Fig. 17. The number of incident photons illuminated on the photocatalyst sheet was measured using a grating spectroradiometer to be 2.9×10^{20} photon h^{-1} (1.7 mA cm^{-2} as the current density if the photon-to-current conversion efficiency was unity).

Solar-to-hydrogen energy conversion efficiency (STH) measurement. The water splitting reaction was carried out under simulated sunlight illumination. The STH is given as

$$\mathrm{STH}\,(\%) = (R(\mathrm{H_2}) \times \Delta G_r)/(P \times S) \times 100 \quad (2)$$

where $R(\mathrm{H_2})$, ΔG_r, P and S denote the rate of hydrogen evolution during the water splitting reaction, the reaction Gibbs energy of the water splitting reaction ($\mathrm{H_2O(l) \rightarrow H_2\,(g) + 1/2\,O_2\,(g)}$), the energy intensity of the AM1.5G solar irradiation (100 mW cm^{-2}) and the irradiated sample area (7.5 cm^2), respectively. Under a pressure of p, bubbles generated on a photocatalyst sheet contain hydrogen and oxygen at pressures of $(2/3)p$ and $(1/3)p$, respectively, if the water pressure is ignored. If hydrogen and oxygen behave as ideal gases, ΔG_r is calculated to be 226, 220, and 220 kJ mol^{-1} at 288 K and 5 kPa, 318 K and 5 kPa, and 331 K and 10 kPa, respectively. The light source used closely approximates the power spectrum of the standard AM1.5G illumination as shown in Supplementary Fig. 18. The energy intensities of the simulated sunlight and the standard AM1.5G were 79.3 and 79.1 mW cm^{-2} over the wavelength range 350–1,100 nm, and 23.2 and 25.5 mW cm^{-2} over 350–540 nm, respectively.